Multirate Resonant Controllers for Grid-Connected Inverters with Harmonic Compensation Function

Xie, Chuan; Zhao, Xin; Li, Kai; Zou, Jianxiao; Guerrero, Josep M.

Published in:
IEEE Transactions on Industrial Electronics

DOI (link to publication from Publisher):
10.1109/TIE.2018.2868249

Publication date:
2019

Document Version
Accepted author manuscript, peer reviewed version

Multirate Resonant Controllers for Grid-Connected Inverters with Harmonic Compensation Function

Chuan Xie, *Member, IEEE*, Xin Zhao, *Member, IEEE*, Kai Li, *Member, IEEE*, Jianxiao Zou, Josep M. Guerrero, *Fellow, IEEE*

***Abstract*—Resonant controller (RSC) is one of the most popular approaches for AC current/voltage control due to the high performance of zero steady-state tracking error. However, it suffers from heavy computational burden issue when multiple RSCs are demanded to control multiple harmonics. To alleviate this issue, a down-sampled multirate RSCs (MRRSCs) scheme is proposed for controlling of power inverters, e.g., grid-connected inverters and active power filters, etc. The proposed control scheme is composed of an inner control loop with a fast sampling rate, which is identical to the switching frequency, and an array of paralleled MRRSCs based external control loop with a reduced sampling rate. With the reduced sample rate, the MRRSCs can be executed alternatively in the *dq*-frame, such that the computational burden can be significantly reduced per cycle. Moreover, to reinforce the wide frequency adaptability of the MRRSC, its central resonant frequency is online updated according to the output of the phase-locked loop (PLL). In the paper, the equivalent single-rate closed-loop model of the overall system is developed, based on which the controller parameters are designed employing the Nyquist diagram and root locus. Finally, experiments are performed on a grid-connected inverter to validate the superiority of the proposed scheme.**

***Index Terms*—Multirate control, resonant control, phase compensation, harmonic compensation, *LCL*-filter.**

I. INTRODUCTION

RESONANT controllers (RSCs), which are based on internal model theory [1], can track sinusoidal references of arbitrary frequencies at both positive and negative sequences with zero steady-state error [2]. They have been applied with satisfactory results to various cases such as distributed renewable energy generation systems [3]–[9], active power filters [10]–[12], and motor drives[13]–[15], etc.

Numerous research about RSCs design has been carried out, and many achievements have been made in past decades. The system delay significantly affects the system stability, thus providing RSC with phase compensation can significantly improve the system stability, especially when dealing with high order harmonics. In [2], one-step and two-step prediction for computational delay compensation are proposed. However, the large phase lag in the control plant is not considered. Thus only low order harmonics (e.g., 5^{th}, 7^{th}, 11^{th}, 13^{th}) can be well controlled. In [10], vector PI (VPI) controller is proposed to compensate the phase lag of the control plant, and the control ability can be extended to 39^{th} order harmonic. However, the VPI is designed from the single *L*-filter model, which may not be suitable for the commonly adopted *LCL*-filtered inverters nowadays. An arbitrary phase angle compensation strategy for RSC is proposed in [16]. In [17], the phase compensation angle of RSC has been elaborately designed in terms of Nyquist diagrams and sensitivity function, and the control plant, computational and pulse-width modulation (PWM) delays have been taken into consideration. It is demonstrated in [17] that the RSCs can be tuned up to the Nyquist frequency by maximizing the distance between the Nyquist trajectory to the critical point. In [18], the similar phase compensation angle has been obtained while in a more simple way.

Since the high gain of RSC resides only in the vicinity of the resonant frequency, the performance of RSC is very sensitive to grid frequency variations, especially with respect to the high order harmonics. The simplest way of decreasing the sensitivity is to increase the RSC gain [13] to enlarge the bandwidth. However, the large RSC gain may deteriorate the system stability margin. A damping term is usually added in an ideal RSC to obtain a non-ideal RSC [3], [19], which may broaden the controller bandwidth. Although the frequency sensitivity of non-ideal RSC may be reduced, the performance is very limited, i.e., ±1Hz [20], [21]. In applications of distributed power generation systems, onboard electric power systems (ships, aircrafts, trains, etc.) or islanded microgrids, where wide range grid frequency variations may occur, e.g., −3~+5 Hz [20]. The performance of both ideal and non-ideal RSCs may degrade dramatically, and online parameter correction is often

Manuscript received May 5, 2018; revised July 16, 2018 and August 7, 2018; accepted August 19, 2018. This work was supported by the National Natural Science Foundation of China under Grant 51807021 and 51707030, and the Sichuan Science and technology support program under Grant 2017GZ0051. (Corresponding author: Chuan Xie.)

C. Xie, K. Li and J. Zou are with the School of Automation Engineering, University of Electronic Science and Technology of China, Chengdu 611731, China (e-mail: {c.xie, jxzou}@uestc.edu.cn; autolikai@gmail.com)

X. Zhao is with the School of Automation, Northwestern Polytechnical University, Xi'an 710072, China (e-mail: xzh@nwpu.edu.cn).

J. M. Guerrero is with the Department of Energy Technology, Aalborg University, Aalborg 9220, Denmark (e-mail: joz@et.aau.dk).

This article has been accepted for publication in a future issue of this journal, but has not been fully edited. Content may change prior to final publication. Citation information: DOI 10.1109/TIE.2018.2868249, IEEE Transactions on Industrial Electronics

necessary to automatically retune the central resonant frequency of RSC to maintain the high control accuracy [11].

RSCs based control scheme will suffer from heavy computational burden when multiple paralleled RSCs are required to control multiple order harmonics simultaneously, e.g., active power filtering [10], [11] and DG inverters with auxiliary harmonic rejection/compensation capability[3], [4]. To reduce the computational burden, reduced order RSCs, i.e., reduced order generalized integrators(ROGIs) or complex controller, are proposed for different applications [21]–[24]. Recently, an adaptive RSC without phase locked loop is proposed in [25] for single phase grid-tied inverters to achieve a simpler and more compact structure. Compared with the traditional single-rate digital control systems, the multirate control systems which consist of more than one sampling frequency have the advantages of less computational burden and flexible sampling frequency selection. The multirate scheme has been successfully applied in repetitive control (RC) in motion control [26]. And a down-sampled multirate RC scheme for constant voltage constant frequency(CVCF) PWM converters and active power filter applications have been investigated in [27], [28]. In light of the benefits can be brought, it has great potential to apply RSCs in a multirate system. The up-sampled multirate RSCs (MRRSCs) scheme is recently proposed in [29] to minimize the deviation of RSC's resonant frequency by increasing the sampling frequency of RSCs via an extra field programmable gate array (FPGA), which inevitably increase the system cost. Unfortunately, the down-sampled MRRSCs is barely studied in the previous publications. Thus, in this paper, the design strategy of down-sampled MRRSCs is investigated.

The rest of the paper is organized as follows. The modeling, stability analysis and parameters tuning criteria of the MRRSCs based closed-loop system are presented in Section II. The experimental testbed is briefly introduced, and the controller design case concerning the power stage parameters of the test bed is given in detail in Section III. Experimental results of harmonic compensation of the grid-connected inverter are provided in Section IV to verify the effectiveness of the proposed scheme. Section V summarizes the paper.

II. Synthesis and Analysis of the MRRSCs Based Closed-Loop System

A. Synthesis of the MRRSCs based closed-loop system

Fig. 1 shows the structure of the MRRSCs based closed-loop system in z-domain. It has an inner control loop with a sampling period of T_s and an external control loop with an array of paralleled MRRSCs. $G_p(z)$ and $C(z)$ represent the transfer function of the control plant and the inner loop controller, respectively. Besides, $R(z)$ is the reference input, $Y(z)$ is the output, $E(z) = R(z)-Y(z)$ is the tracking error, and $D(z)$ is the disturbance.

The paralleled MRRSCs has an increased sampling period of $T_m = mT_s$, m is a positive integer. The relationship between the two sampling periods can be expressed as:

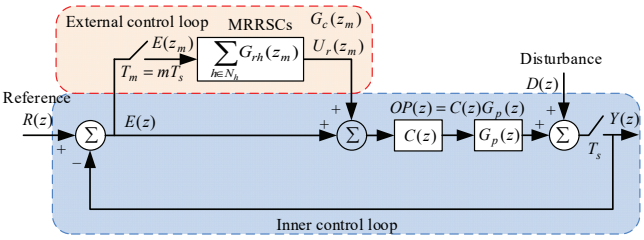

Fig. 1. The structure of the MRRSCs based closed-loop system.

$$T_m = mT_s, z = e^{sT_s}, z_m = z^m = e^{sT_m} \tag{1}$$

When m = 1, the MRRSC becomes the conventional single-rate RSC. In the MRRSCs block, $E(z_m)$ is the down-sampled error signal. And $U_r(z_m)$ is the output of MRRSCs, which is interpolated by a zero-order-hold (ZOH) block.

Phase compensation of RSC can significantly improve the closed-loop system stability margin, and it is especially necessary for the RSC aiming at controlling high order harmonics [11]. Thus, in this paper, the phase compensated MRRSC is used. The z-domain transfer function of the MRRSC can be expressed as (2), which is discretized from the corresponding s-domain transfer function via Tustin with prewarping [3].

$$G_{rh}(z_m) = K_{Ih}\frac{a_0 + a_1 z_m^{-1} + a_2 z_m^{-2}}{1 + b_1 z_m^{-1} + z_m^{-2}} \tag{2}$$

where $a_0 = [\sin(h\omega_1 T_m+\varphi_h)-\sin(\varphi_h)]/(h\omega_1)$, $a_1 = [\cos(h\omega_1 T_m)-1]\sin(\varphi_h)/(h\omega_1)$, $a_2 = [-\sin(h\omega_1 T_m-\varphi_h)-\sin(\varphi_h)]/(2h\omega_1)$, $b_1 = -2\cos(h\omega_1 T_m)$, h is harmonic order, ω_1 is the fundamental angular frequency, K_{Ih} is the integral gain and φ_h is the phase compensation angle. $G_{rh}(z_m)$ provides infinite gain at the resonant angular frequency $h\omega_1$, which ensures zero steady-state error tracking at $h\omega_1$. The transfer function of the multirate controller $G_c(z_m)$, which consists of multiple MRRSCs, can be expressed as

$$G_c(z_m) = \frac{U_r(z_m)}{E(z_m)} = \sum_{h\in N_h} G_{rh}(z_m) \tag{3}$$

where N_h is the set of selected harmonic orders.

According to Fig. 1, the open-loop transfer function of the inner control loop can be derived as:

$$OP(z) = C(z)G_p(z) \tag{4}$$

B. Equivalent single-rate closed-loop system

To analyze the MRRSCs based closed-loop system in Fig. 1, it is transformed into an equivalent single rate system with a sampling rate equals to the RSC sampling rate as shown in Fig. 2. In the figure, $\overline{OP}(z_m)$ represents the RSC sampling rate counterpart of OP(z).

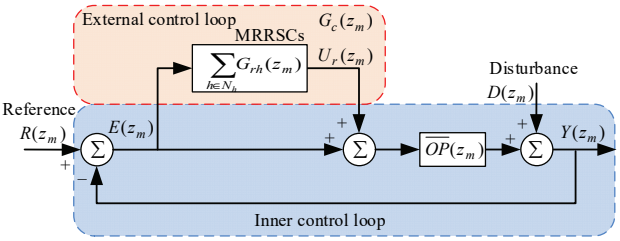

Fig. 2. Equivalent single-rate RSCs based closed-loop system.

This article has been accepted for publication in a future issue of this journal, but has not been fully edited. Content may change prior to final publication. Citation information: DOI 10.1109/TIE.2018.2868249, IEEE Transactions on Industrial Electronics

In order to develop the equivalent RSC sampling rate model of the inner control loop open-loop transfer function, (4) is rewritten in state-space form as follows [30]:

$$\begin{cases} x_f(k+1) = A_f x_f(k) + B_f u_f(k) \\ y_f(k) = C_f x_f(k) + D_f v_f(k) \end{cases} \tag{5}$$

where x_f, u_f, y_f, and v_f are the state variables, input, output, and disturbance, respectively. And A_f, B_f, C_f, and D_f are system matrix, input matrix, output matrix and feedforward matrix, respectively.

Since the sampling rate of RSC is m times slower than that of the inner control loop, the RSC uses both the present and previous m steps output signals of the inner loop to produce an output at present instant. Note that the discrete time index k corresponding to the RSC sampling rate. For (5), $k = mK + i$ (i =0, 1, 2, . . . $m-1$), the state-space equation in one RSC rate sampling period mT_s can be expressed as [26], [27]:

$$\begin{cases} x_f(Km+1) = A_f x_f(Km) + B_f u_f(Km) \\ x_f(Km+2) = A_f x_f(Km+1) + B_f u_f(Km) \\ \vdots \\ x_f(Km+m) = A_f x_f(Km+m-1) + B_f u_f(Km) \end{cases} \tag{6}$$

According to (6), the down-sampled state-space equation can be rewritten as follows:

$$\begin{cases} x_s(K+1) = A_s x_s(K) + B_s u_s(K) \\ y_s(K) = C_s x_s(K) + D_s v_s(K) \end{cases} \tag{7}$$

where $A_S = A_f^m$, $B_S = (A_f^{m-1}B_f + A_f^{m-2}B_f + \cdots + A_fB_f + B_f)$, $C_s = C_f$ and $D_s = D_f$. The equivalent RSC sampling rate open-loop and closed-loop transfer functions of the inner control loop can be derived as:

$$\overline{OP}(z_m) = C_s(z_m I - A_s)^{-1} B_s . \tag{8}$$

$$\overline{CP}(z_m) = \overline{OP}(z_m)/[1 + \overline{OP}(z_m)] . \tag{9}$$

C. System stability analysis

Based on (3), (8) and (9), the open-loop and closed-loop transfer functions of the overall equivalent single-rate system can be derived as

$$T_o(z_m) = [1 + G_c(z_m)] \cdot \overline{OP}(z_m) \tag{10}$$

$$T_c(z_m) = \frac{T_o(z_m)}{1 + T_o(z_m)} = \frac{[1 + G_c(z_m)] \cdot \overline{OP}(z_m)}{1 + [1 + G_c(z_m)] \cdot \overline{OP}(z_m)} = \frac{\overline{OP}(z_m)}{1 + \overline{OP}(z_m)} \cdot \frac{[1 + G_c(z_m)]}{1 + G_c(z_m)\overline{CP}(z_m)} \tag{11}$$

From (11), it can be observed that the overall closed-loop system is stable if the following two conditions hold [18]:

i) the roots of $1 + \overline{OP}(z_m) = 0$ are inside the unit circle,

ii) the roots of $1 + G_c(z_m)\overline{CP}(z_m) = 0$ are also inside the unit circle.

The first stability condition can be easily achieved by tuning the inner control loop, which has been well presented. The second system stability condition can be inspected by applying the Nyquist stability criterion to its equivalent open-loop transfer function, i.e., $G_c(z_m)\overline{CP}(z_m)$. According to the Nyquist stability criterion, the number of the open-loop unstable poles P must equal to N, which stands for the net number of counter-clockwise encirclements of the critical point (-1, j0) on the Nyquist diagram, to ensure system stability, i.e., $P = N$ [30]. In case $P = 0$ the distance between the Nyquist curve and the critical point (-1, j0) provides a clear indication of stability margin [17].

D. MRRSCs parameters design criteria

Selecting the down-sampled sampling rate is very important for designing a multirate system, it should be the first step before further designing the parameters of MRRSC. According to the Nyquist-Shannon sampling theorem, a sufficient sample-rate for a given signal to be handled is at least two times of its bandwidth. If the frequency of the signal to be controlled is too close to Nyquist frequency, the accuracy of producing the corresponding control signal will drop. Consequently, the control accuracy degrades. Thus, m should not be too large, and it should be properly chosen taking into consideration following three aspects: i) bandwidth of signals to be controlled, ii) reduction of computational burden and iii) degradation of controller performance.

The phase compensation angle of MRRSC is set equal to the phase delay of the equivalent control plant [18], viz., (12), so that the distance between the Nyquist trajectory and the critical point can be maximized, which implies the highest stability and avoidance of closed-loop anomalous peaks, and a significant improvement in transient response (greater damping) [17].

$$\varphi_h = -\angle\overline{CP}(e^{jh\omega_1 T_m}) \tag{12}$$

where φ_h is the phase compensation angle of MRRSC tuned at h^{th} order harmonic.

The second stability condition also relies on the value of the integral gain of MRRSC. For the sake of simplicity, the integral gains of the selected MRRSCs, i.e., K_{Ih}, are set to be identical to each other. To calculate an optimal analytical value of K_{Ih} is difficult due to the high order of the system. Thus, here only the range of K_{Ih} regarding system stability is determined by employing the root locus of the closed-loop system, i.e., $1 + G_c(z_m)\overline{CP}(z_m)$. Considering the more closely the root locus approaching the unit circle, the smaller the system damping coefficient will be, which implies more easily prone to system oscillation. Thus, the tradeoff should be made between the system stability and dynamic response speed when selecting the value of K_{Ih}.

III. MRRSCs BASED CURRENT CONTROL STRATEGY

To evaluate the performance of the proposed MRRSCs scheme, a three-phase compact lab-scale islanded microgrid, which consists of two *LCL*-filtered inverters, is built in the laboratory and the corresponding block diagram is shown in Fig. 3. The left side converter serves as a grid-forming inverter, while the other one acts as a grid-connected inverter with the proposed control strategy. A diode rectifier is connected to the AC bus to emulate the nonlinear load. The power stage parameters are listed in Table I for the controller parameters design.

This article has been accepted for publication in a future issue of this journal, but has not been fully edited. Content may change prior to final publication. Citation information: DOI 10.1109/TIE.2018.2868249, IEEE Transactions on Industrial Electronics

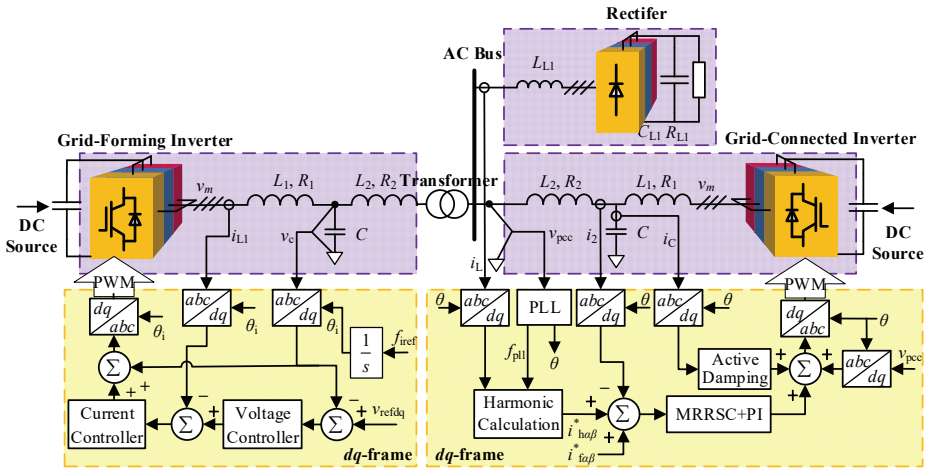

Fig. 3. Equivalent single-line diagram of the built compact lab-scale islanded microgrid test bed in the laboratory.

TABLE I
POWER STAGE PARAMETERS

	Symbol	Quantity	Value
Inverters	L_1	Converter side inductor	2.2 mH
	R_1	parasitic resistance of L_1	0.1 Ω
	L_2	Grid side inductor	2.2 mH
	R_2	parasitic resistance of L_1	0.1 Ω
	C	Capacitor of LCL-filter	10 μF
Nonlinear load	L_{L1}	input inductor	2.2 mH
	C_{L1}	DC-link Capacitor	165 μF
	R_{L1}	Load resistance	150 Ω

A. Inner control loop design

Fig. 4 shows the block diagram of the inner control loop in z-domain, where the capacitor current feedback based active damping (AD) is used to address the LCL filter resonance issue, and the inner loop controller C(z) employs a PI controller to regulate the output current i_2. The computational delay has been modeled as one sampling period delay. The corresponding z-domain plant transfer functions are derived as [31]:

$$G_{m2}(z)=\frac{i_2(z)}{v_m(z)}$$

$$=\frac{\omega_r T_s[z^2-2\cos(\omega_r T_s)z+1]-\sin(\omega_r T_s)(z-1)^2}{\omega_r[L_1+L_2](z-1)[z^2-2\cos(\omega_r T_s)z+1]} \quad (13)$$

$$G_{mc}(z)=\frac{i_c(z)}{v_m(z)}=\frac{\sin(\omega_r T_s)}{\omega_r L_1}\cdot\frac{z-1}{z^2-2\cos(\omega_r T_s)z+1} \quad (14)$$

where $\omega_r=\sqrt{(L_1+L_2)/(L_1L_2C_f)}$ is the resonance angular frequency. Note that $G_{m2}(z)$ and $G_{mc}(z)$, which stand for the transfer z-domain functions of inverter output v_m to the grid side current i_2 and the capacitor current i_c respectively, are discretized from their corresponding s-domain ones via ZOH to reflect the PWM delay.

In Fig. 4, $D(z)$ stands for the lead-lag compensator, which is used to compensate the delay of AD loop, is expressed as

$$D(z)=K_{ad}\frac{z-1}{z-0.5}. \quad (15)$$

where K_{ad} represents the active damping loop gain.

In the paper, the backward Euler integration is used in the PI regulator, which is expressed as

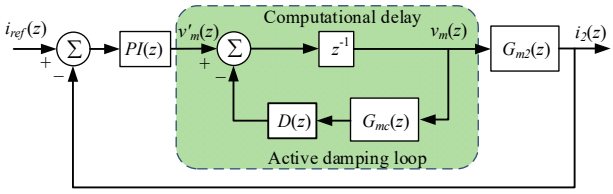

Fig. 4. Block diagram of the inner control loop in z-domain [31].

$$PI(z)=K_P+K_I T_s\frac{z}{z-1}. \quad (16)$$

where K_P and K_I represent the proportional and the integral gains, respectively.

Since designing of inner control loop parameters, i.e., active damping compensator and PI controller, are already well presented [31], they won't be discussed in this paper. The tuned inner control loop parameters are directly listed in Table II for further MRRSCs parameters design.

Substituting the parameters listed in Table I and II into equations (13) to (16), the open-loop and closed-loop transfer functions of the inner control loop can be derived as (17) and (18) which are given at the bottom of the next page.

The Bode plots of $OP(z)$ and $CP(z)$ are shown in Fig. 5, both sufficient phase margins (PMs) and smooth magnitude characteristic of the closed-loop are achieved. It implies inner control loop parameters are well designed. Nonetheless, the harmonic control capability of the system is very limited, due to the large phase lag in the high-frequency range, e.g., the 90º phase lag at 400 Hz. To reinforce the system harmonic control capability, external MRRSCs regarding dominant harmonic components (6^{th}, 12^{th}, 18^{th}) are added.

TABLE II
TUNED PARAMETERS OF THE INNER CONTROL LOOP

Symbol	Quantity	Value
K_{ad}	AD gain	6
K_P	Proportional gain	10
K_I	Integral gain	314
T_s	Sampling period	100 μs

This article has been accepted for publication in a future issue of this journal, but has not been fully edited. Content may change prior to final publication. Citation information: DOI 10.1109/TIE.2018.2868249, IEEE Transactions on Industrial Electronics

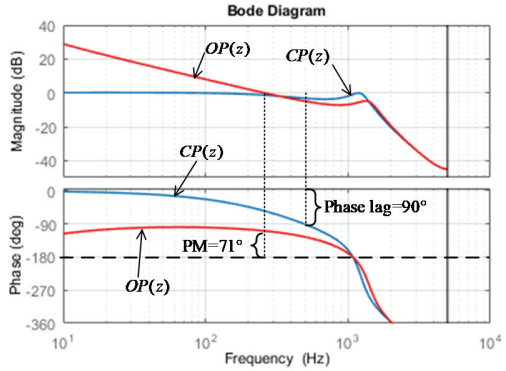

Fig. 5. Bode plots of the open-loop and closed-loop transfer functions.

B. External loop MRRSC parameters design

In this case, the MRRSCs is implemented in the *dq*-frame, and the highest order harmonic to be controlled is 18th order; thus the sampling rate should be no less than 1.8 kHz (viz., *m* should be smaller than 5.5), according to the design criterion in Section II.D. Hereinafter, the MRRSCs with different sampling rates, i.e., *m*=1, 2, 4, will be designed for comparative study.

According to (4) to (9), the equivalent single-rate closed-loop transfer function $\overline{CP}(z_m)$ under different RSC sampling rates (m = 1, 2, 4) are derived as (19) which also is given at the bottom of next page.

The phase compensation angles for the MRRSCs tuned at 6th, 12th and 18th order harmonics are calculated according to (12) and (19), and the results are listed in TABLE III.

The root loci of the closed-loop system $1+G_c(z_m)\overline{CP}(z_m)$ under different RSC sampling rates are depicted in Fig. 6, and the corresponding zoomed-in diagram is depicted in Fig. 7. In the studied case, the upper boundaries of K_{Ih} under different RSC sampling rates (m=1, 2, 4) exist at the same place in Fig. 7, the smallest value of K_{Ihmax} equals to 1200. Finally, the MRRSCs integral gains are set equal to 500 for all sampling rates to guarantee sufficient stability margin.

TABLE III
PHASE COMPENSATION ANGLES FOR MRRSCS

Harmonic order	Compensation angles (radians)		
	m=1	*m*=2	*m*=4
6	1.01	1.07	1.21
12	1.68	1.91	2.77
18	2.45	2.97	4.56

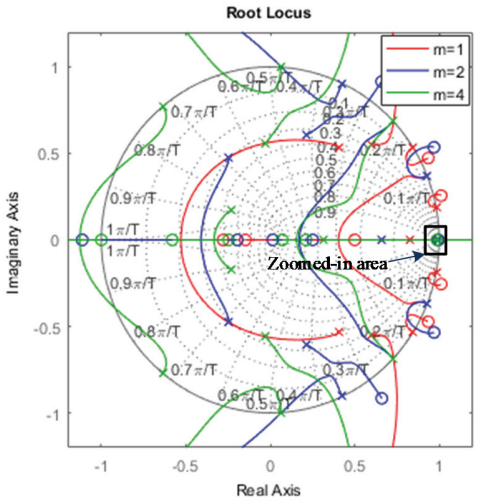

Fig. 6. Root loci of $1+G_c(z_m)\overline{CP}(z_m)$ under different RSC sampling rates.

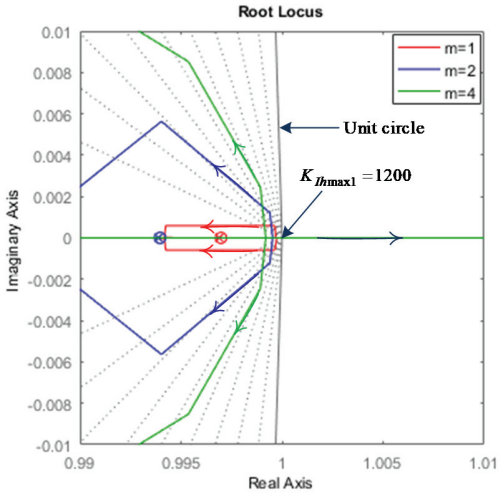

Fig. 7.Zoomed-in location in Fig. 6.

With the designed parameters for both inner and external control loop, the pole diagram of the overall closed-loop system, i.e., Eq. (11), is drawn in Fig. 8 to check the system stability. It can be seen from Fig. 8 that above-designed parameters ensure the stability of the overall closed-loop system since all the poles of the closed-loop transfer function stay inside of the unit circle.

$$OP(z)=\frac{PI(z)z^{-1}G_{m2}(z)}{1+z^{-1}D(z)G_{mc}(z)}=\frac{0.0173z^4+0.04095z^3-0.07414z^2+0.007421z+0.008626}{z^6-3.856z^5+6.633z^4-6.683z^3+4.135z^2-1.471z+0.2428} \tag{17}$$

$$CP(z)=\frac{0.0173z^4+0.04095z^3-0.07414z^2+0.007421z+0.008626}{z^6-3.856z^5+6.65z^4-6.642z^3+4.061z^2-1.464z+0.2514} \tag{18}$$

$$\overline{CP}(z_m)=\begin{cases}\dfrac{0.0173z^4+0.0410z^3-0.0741z^2+0.0074z+0.0086}{z^6-3.856z^5+6.65z^4-6.642z^3+4.061z^2-1.464z+0.2514}, m=1\\ \dfrac{0.0173z_2^5+0.3062z_2^4-0.0006z_2^3-0.3536z_2^2+0.0178z_2+0.0166}{z_2^6-1.586z_2^5+1.029z_2^4-0.6757z_2^3+0.2992z_2^2-0.1388z_2+0.0755}, m=2\\ \dfrac{0.3512z_4^5+0.3814z_4^4-0.3400z_4^3-0.3396z_4^2-0.0398z_4+0.0046}{z_4^6-0.773z_4^5+0.0453z_4^4-0.2356z_4^3-0.0395z_4^2+0.0126z_4+0.0081}, m=4\end{cases} \tag{19}$$

This article has been accepted for publication in a future issue of this journal, but has not been fully edited. Content may change prior to final publication. Citation information: DOI 10.1109/TIE.2018.2868249, IEEE Transactions on Industrial Electronics

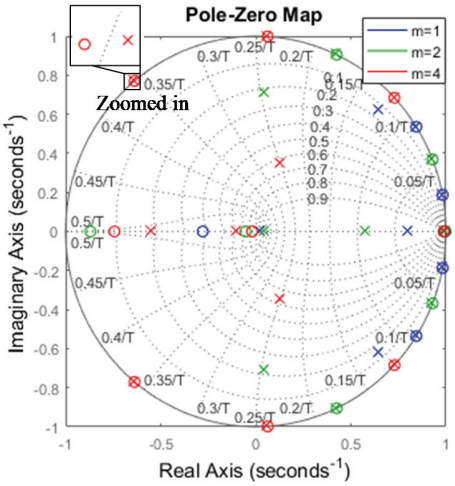

Fig. 8.Pole diagram of the overall closed-loop system with tuned controller parameters.

The pole diagram of the closed-loop system with insufficient phase compensation for MRRSCs is also exemplified in Fig. 9 to illustrate the effect of phase compensation accuracy on the system stability. The reduced sampling rate will increase the delay, thus larger phase compensation angles are required for MRRSCs with large m as listed in TABLE III. When applying the compensation angles for MRRSCs with m=1 to the one with m=4, the phase compensation is not enough, and the overall closed-loop system will go into instability as the pole corresponding to higher order harmonic, i.e., 18th order harmonic, will go outside of the unit circle as shown in Fig. 9.

To improve the frequency adaptability of MRRSCs, a phase-locked loop (PLL) is used to update the central resonant frequencies of MRRSCs. It can be seen from (2) that all the four coefficients of MRRSC are relevant to its resonant angular frequency $h\omega_1$. However, only the coefficient b_1, which affects the poles of MRRSC, is online corrected as shown in Fig. 10, for the sake of simplicity and less computational burden. This simplicity inevitably leads to the phase compensation error.

The phase compensation error as a function of the phase compensation angle and frequency variation $\Delta\omega_1$ is shown in the Fig. 11. It can be seen that the phase compensation errors of MRRSCs (m=2) tuned at 6th, 12th and 18th order harmonics in the presence of ±10% frequency variations are no larger than 0.05 radians, which are very small and can be ignored. The same results can be obtained for m = 1 and m = 4.

The robustness of the overall closed-loop system to parameter variations, i.e., inductance variations, has been further analyzed. Taking m = 4 for example, the system pole diagram in presence of ±10% inductance variations is drawn in Fig. 12, where all the poles of the closed-loop transfer function stay inside of the unit circle. The same results can be obtained for m = 1 and m = 2.

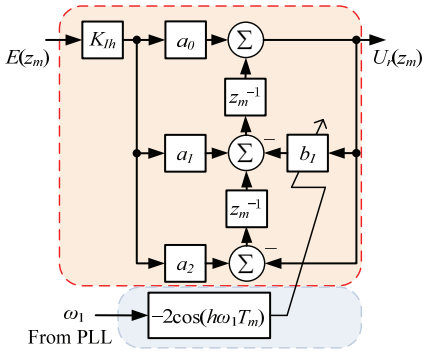

Fig. 10. Implementation of the PLL-based frequency adaptive MRRSC with direct form II transpose (DFIIt) structure[3].

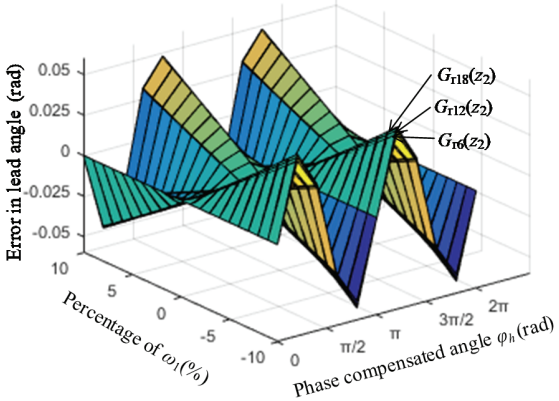

Fig. 11. Phase compensation error as a function of phase compensation angle and frequency variation $\Delta\omega_1$.

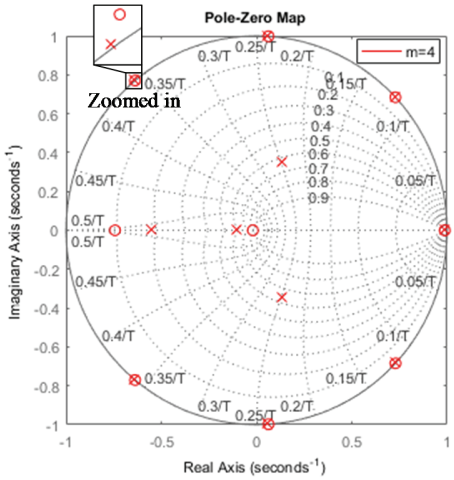

Fig. 9. Pole diagram of the overall closed-loop system with insufficient phase compensation.

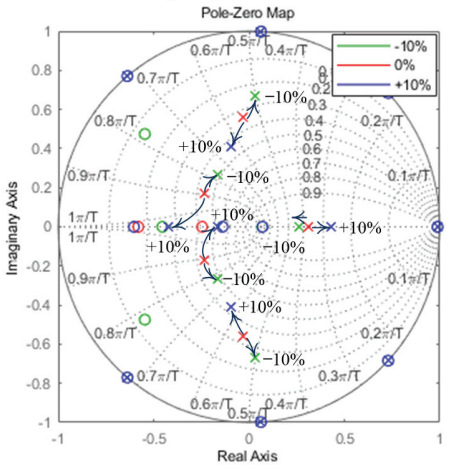

Fig. 12. Pole diagram of the overall closed-loop system in presence of ± 10% inductance variations.

This article has been accepted for publication in a future issue of this journal, but has not been fully edited. Content may change prior to final publication. Citation information: DOI 10.1109/TIE.2018.2868249, IEEE Transactions on Industrial Electronics

IV. Experimental Results

Fig. 13 shows the experimental setup. Two 2.2-kW *Danfoss* inverters are used as the grid-forming inverter and grid -connected inverter, respectively. The control algorithm is applied in dSPACE 1005 with a 10 kHz sampling frequency. To validate the performance of the proposed MRRSCs scheme, the grid-connected inverter is utilized to compensate the harmonics generated by the non-linear load. The experimental data are all recorded by the Tektronix TPS2024B Oscilloscope.

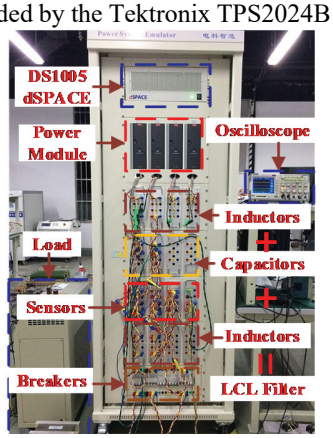

Fig. 13. Hardware picture for the experimental setup.

The computational burden of the MRRCS is analyzed in number of operations. This is commonly regarded as valid for assessing the computational burden without further experimental verification [32], [33]. It's evident that each RSC requires 5 multiplications and 5 additions as shown in Fig. 10. Then the total computational burden of the MRRCS is proportional to the number of required RSCs. Taking m=2 for example, the MRRSCs, i.e., $G_c(z_m)$, is alternatively executed in the dq-frame as shown in Fig. 14, $G_c(z_m)$ in d-axis is executed only at odd sampling points while $G_c(z_m)$ in q-axis is executed only at even sampling points. Consequently, the computational burden of RSCs at each cycle can be reduced to only half of that in a full rate system.

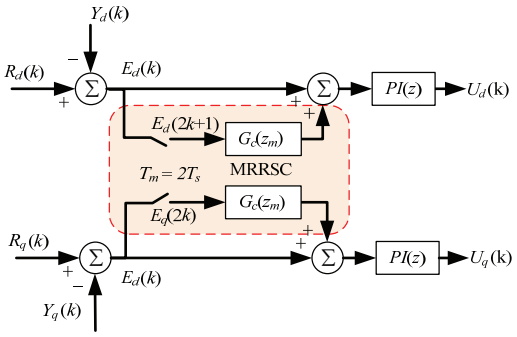

Fig. 14. Implementation of MRRSCs in the dq-frame (m=2).

C. Harmonic compensation performance under different RSC sampling rates

To evaluate the steady-state performance at different RSC sampling rates, the corresponding steady-state waveforms are given in Fig. 15. From up to bottom are grid current, load current, inverter output current, and current tracking error. It can be seen that the load current, which is highly distorted, has been compensated by the inverter, and makes the grid current very close to being sinusoid after compensation. The compensated grid current with MRRSCs at different RSC rates are comparable so that it is hard to tell the difference between them. Thus, fast Fourier transformation (FFT) analysis of both load and grid currents are given in Fig. 16 to further evaluate the controller performance. It can be observed from Fig. 16 that the total harmonic distortion (THD) of the grid has been attenuated from 58% to below 6%. Note that the THD calculation in this paper is from 2nd up to 50th order harmonics. The MRRSC with reduced sampling frequency will more or less sacrifice the performance to some extent at higher order harmonics because of the approaching to the Nyquist frequency and precision degradation of producing the control output for high order harmonics.

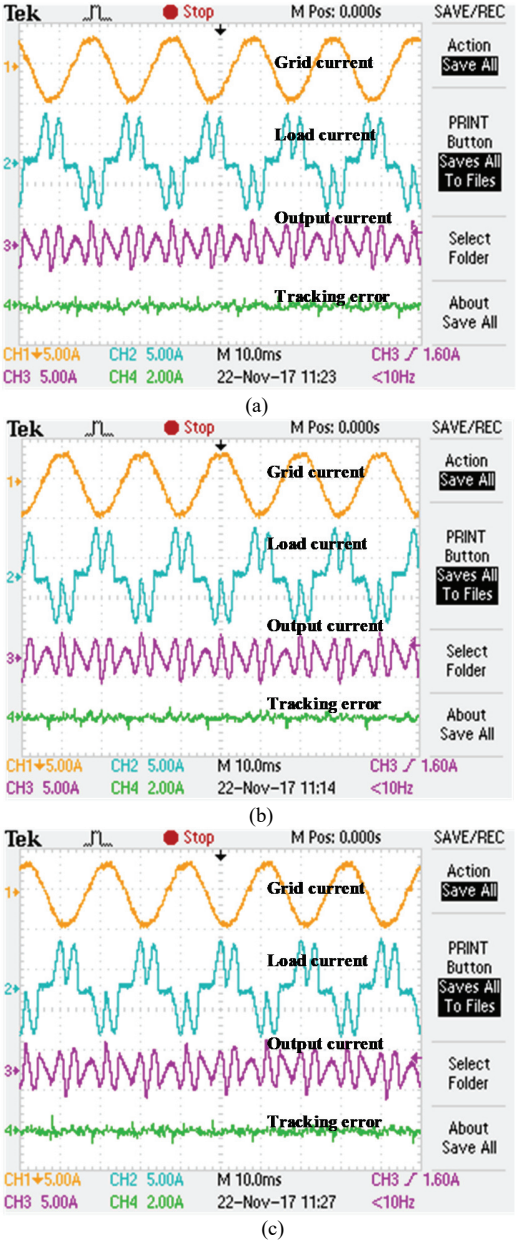

Fig. 15. Experimental results of harmonic compensation under different RSC sampling rates. (a) m = 1, (b) m = 2, (c) m = 4.

This article has been accepted for publication in a future issue of this journal, but has not been fully edited. Content may change prior to final publication. Citation information: DOI 10.1109/TIE.2018.2868249, IEEE Transactions on Industrial Electronics

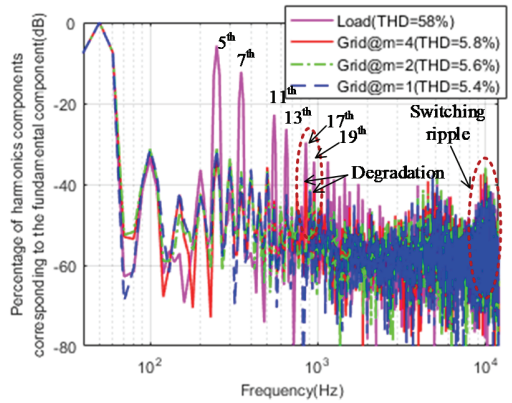

Fig. 16. Spectra of load and grid currents under different RSC sampling rates.

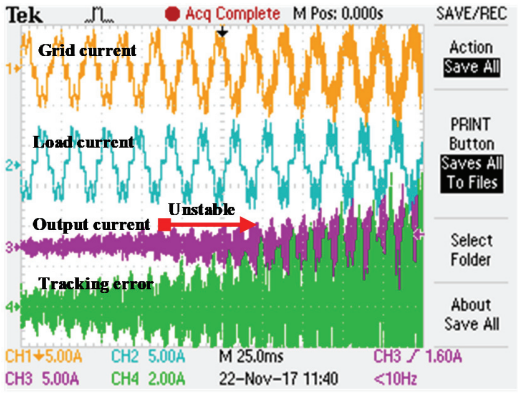

Fig. 17. Experimental results under change of MRRSC phase compensation angle from m=1 to m=4).

The impact of phase compensation on the system stability is also verified, and the results are shown in Fig. 17. Note that the MRRSCs are operated with sampling frequency equals to 2.5 kHz, viz., m=4. When changing the compensation angles of the MRRSCs from the ones for m=4 to the ones for m=1 as listed in Table III, the output current of the inverter starts to oscillate, and the system becomes unstable.

D. Harmonic compensation performance under wide grid frequency variation (m = 2)

To evaluate the frequency adaptivity of the MRRSC, experiments are carried out when the RSC sampling rate is set to 5 kHz (m = 2). Fig. 18 illustrates the spectra of load and grid currents under different grid frequencies, i.e. 45Hz and 55Hz. The THD of grid currents with MRRSCs under different grid frequencies are also been compensated to below 6% and are comparable to the one at the rated grid frequency as shown in Fig. 16, this indicates that adaptive MRRSCs have good frequency adaptivity under wide grid frequency variations.

E. Dynamic performance of harmonic compensation under different RSC sampling rates

The transient waveforms of harmonic compensation are given in Fig. 19 to evaluate the dynamic performance of MRRSCs at different RSC sampling rates. It can be seen that before activating the harmonic compensation, the grid current is almost identical to the load current. After enabling the harmonic compensation function, the concerned harmonic components are compensated, and consequently, the harmonic distortion of the grid current is reduced significantly. Due to the amplification of the harmonic when implementing the harmonic compensation to capacitive nonlinear load [34], it is unfair to evaluate the response of the controller via the time within which the output reached the steady-state. Thus, the dynamic performance is evaluated via the tracking error convergence speed after activating the harmonic compensation function. It can be seen from Fig. 19 that the error convergence time is about 0.01s for different RSC sampling rates. Since the integral gains of the MRRSCs with different RSC sampling rates are identical, dynamic response speeds of MRRSCs at different RSC sampling rates are similar. It can be concluded that the multirate scheme in fact barely degrades the dynamic characteristics of the RSC.

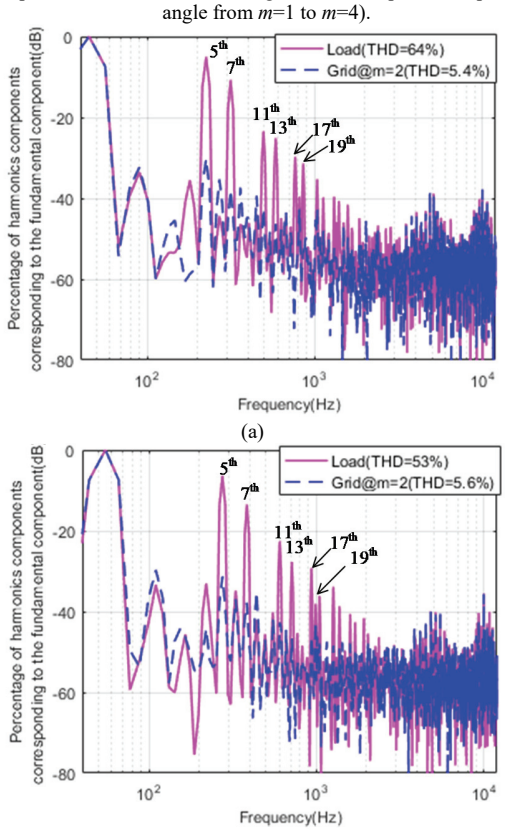

Fig. 18. Spectra of load and grid currents under different grid frequencies. (a) 45 Hz, (b) 55 Hz.

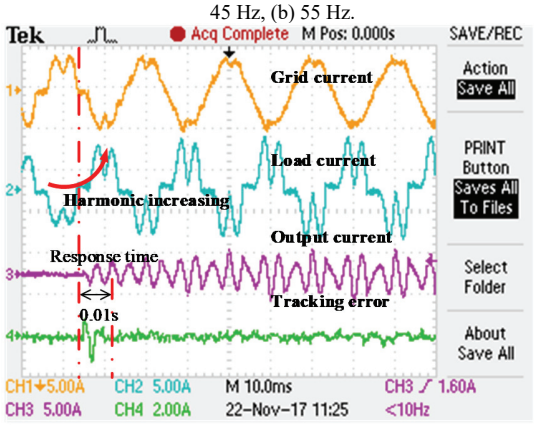

(a)

This article has been accepted for publication in a future issue of this journal, but has not been fully edited. Content may change prior to final publication. Citation information: DOI 10.1109/TIE.2018.2868249, IEEE Transactions on Industrial Electronics

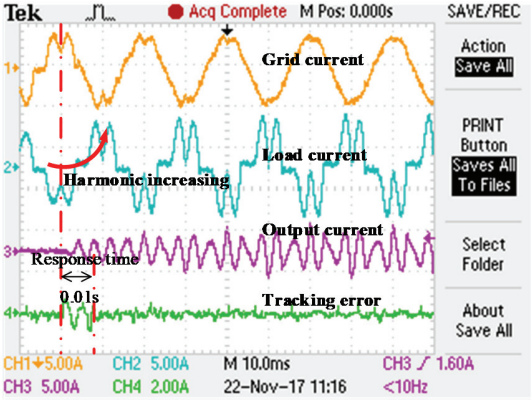

(b)

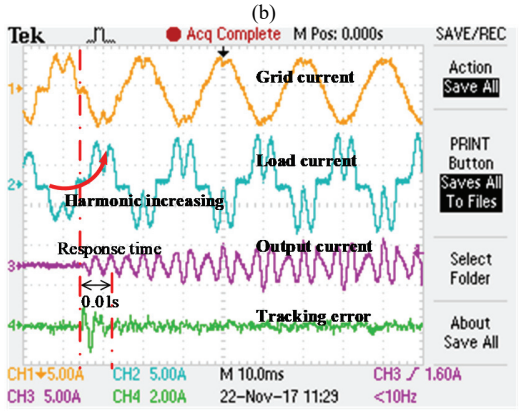

(c)

Fig. 19. Transient experimental waveforms of harmonic compensation at different RSC sampling rates. (a) $m = 1$, (b) $m = 2$, (c) $m = 4$.

V. Conclusion

This paper proposes an MRRSCs scheme for three-phase grid-tie inverters with harmonic compensation function. The main advantages of the proposal are: i) with the PLL-based phase compensated RSCs, high harmonic control precision can be achieved even in the presence of wide range grid frequency variations,e.g., islanded microgrids occasions; ii) with multirate technique, the computational burden of the paralleled RSCs can be reduced significantly at the cost of little steady stated performance degradation; iii) multirate scheme doesn't change the dynamic performance of RSCs; thus a faster dynamic response speed can be achieved compared with multirate repetitive controller. Thus, the proposed approach is not only suitable for embedding grid-connected inverters with harmonic compensation capability but also can be extended to design a cost-effective control system for active power filter applications.

References

[1] S. Fukuda and T. Yoda, "A Novel Current-Tracking Method for Active Filters Based on a Sinusoidal Internal Model," *Ind. Appl. IEEE Trans. On*, vol. 37, no. 3, pp. 888–895, May 2001.

[2] X. Yuan, W. Merk, H. Stemmler, and J. Allmeling, "Stationary-Frame Generalized Integrators for Current Control of Active Power Filters with Zero Steady-State Error for Current Harmonics of Concern Under Unbalanced and Distorted Operating Conditions," *Ind. Appl. IEEE Trans. On*, vol. 38, no. 2, pp. 523–532, Mar. 2002.

[3] R. Teodorescu, F. Blaabjerg, M. Liserre, and P. C. Loh, "Proportional-Resonant Controllers and Filters for Grid-Connected Voltage-Source Converters," *Electr. Power Appl. IEE Proc.*, vol. 153, no. 5, pp. 750–762, Sep. 2006.

[4] J. He, Y. W. Li, and F. Blaabjerg, "Flexible Microgrid Power Quality Enhancement Using Adaptive Hybrid Voltage and Current Controller," *IEEE Trans. Ind. Electron.*, vol. 61, no. 6, pp. 2784–2794, Jun. 2014.

[5] X. Guo, Y. Yang, and X. Zhang, "Advanced Control of Grid-Connected Current Source Converter Under Unbalanced Grid Voltage Conditions," *IEEE Trans. Ind. Electron.*, vol. 65, no. 12, pp. 9225–9233, Dec. 2018.

[6] Q. Wang, M. Cheng, Y. Jiang, W. Zuo, and G. Buja, "A Simple Active and Reactive Power Control for Applications of Single-Phase Electric Springs," *IEEE Trans. Ind. Electron.*, vol. 65, no. 8, pp. 6291–6300, Aug. 2018.

[7] J. Meng, W. Wang, X. Tang, and X. Xu, "Zero-sequence voltage trajectory analysis for unbalanced distribution networks on single-line-to-ground fault condition," *Electr. Power Syst. Res.*, vol. 161, no. 8, pp. 17–25, Apr. 2018.

[8] X. Guo, Y. Yang, and T. Zhu, "ESI: A Novel Three-Phase Inverter With Leakage Current Attenuation for Transformerless PV Systems," *IEEE Trans. Ind. Electron.*, vol. 65, no. 4, pp. 2967–2974, Apr. 2018.

[9] K. Li, M. Wei, C. Xie, F. Deng, J. M. Guerrero, and J. C. Vasquez, "Triangle Carrier based Discontinuous PWM for Three-Level NPC Inverters," *IEEE J. Emerg. Sel. Top. Power Electron.*, vol. PP, no. 99, pp. 1–1, 2018. DOI: 10.1109/JESTPE.2018.2812704.

[10] C. Lascu, L. Asiminoaei, I. Boldea, and F. Blaabjerg, "High Performance Current Controller for Selective Harmonic Compensation in Active Power Filters," *IEEE Trans. Power Electron.*, vol. 22, no. 5, pp. 1826–1835, Sep. 2007.

[11] A. G. Yepes, F. D. Freijedo, O. Lopez, and J. Doval-Gandoy, "High-Performance Digital Resonant Controllers Implemented With Two Integrators," *IEEE Trans. Power Electron.*, vol. 26, no. 2, pp. 563–576, Feb. 2011.

[12] Y. Tang, P. C. Loh, P. Wang, F. H. Choo, F. Gao, and F. Blaabjerg, "Generalized Design of High Performance Shunt Active Power Filter With Output LCL Filter," *IEEE Trans. Ind. Electron.*, vol. 59, no. 3, pp. 1443–1452, Mar. 2012.

[13] D. N. Zmood and D. G. Holmes, "Stationary Frame Current Regulation of PWM Inverters with Zero Steady-State Error," *IEEE Trans. Power Electron.*, vol. 18, no. 3, pp. 814–822, May 2003.

[14] C. Xia, B. Ji, and Y. Yan, "Smooth Speed Control for Low-Speed High-Torque Permanent-Magnet Synchronous Motor Using Proportional-Integral-Resonant Controller," *IEEE Trans. Ind. Electron.*, vol. 62, no. 4, pp. 2123–2134, Apr. 2015.

[15] Z. Gong, X. Wu, P. Dai, and R. Zhu, "Modulated Model Predictive Control for MMC-based Active Front-End Rectifiers Under Unbalanced Grid Conditions," *IEEE Trans. Ind. Electron.*, pp. 1–11, 2018. DOI: 10.1109/TIE.2018.2844836.

[16] P. Mattavelli, "Synchronous-Frame Harmonic Control for High-Performance AC Power Supplies," *IEEE Trans. Ind. Appl.*, vol. 37, no. 3, pp. 864–872, May 2001.

[17] A. G. Yepes, F. D. Freijedo, O. Lopez, and J. Doval-Gandoy, "Analysis and Design of Resonant Current Controllers for Voltage-Source Converters by Means of Nyquist Diagrams and Sensitivity Function," *IEEE Trans. Ind. Electron.*, vol. 58, no. 11, pp. 5231–5250, Nov. 2011.

[18] C. Xie, X. Zhao, K. Li, J. Zou, and M. G. Josep, "A New Tuning Method of Multi-Resonant Current Controllers for Grid-Connected Voltage Source Converters," *IEEE J. Emerg. Sel. Top. Power Electron.*, vol. pp, no. 99, pp. 1–1, 2018. DOI: 10.1109/JESTPE.2018.2833806.

[19] M. Castilla, J. Miret, J. Matas, L. G. de Vicuna, and J. M. Guerrero, "Control Design Guidelines for Single-Phase Grid-Connected Photovoltaic Inverters With Damped Resonant Harmonic Compensators," *IEEE Trans. Ind. Electron.*, vol. 56, no. 11, pp. 4492–4501, Nov. 2009.

[20] A. V. Timbus, M. Ciobotaru, R. Teodorescu, and F. Blaabjerg, "Adaptive Resonant Controller for Grid-Connected Converters in Distributed Power Generation Systems," in *Twenty-First Annual IEEE Applied Power Electronics Conference and Exposition, 2006. APEC '06.*, 2006, pp. 1601–1606.

[21] S. Gomez Jorge, C. A. Busada, and J. A. Solsona, "Frequency-Adaptive Current Controller for Three-Phase Grid-Connected Converters," *IEEE Trans. Ind. Electron.*, vol. 60, no. 10, pp. 4169–4177, Oct. 2013.

[22] C. A. Busada, S. Gomez Jorge, A. E. Leon, and J. A. Solsona, "Current Controller Based on Reduced Order Generalized Integrators for Distributed Generation Systems," *IEEE Trans. Ind. Electron.*, vol. 59, no. 7, pp. 2898–2909, Jul. 2012.

[23] X. Guo and J. M. Guerrero, "General Unified Integral Controller with Zero Steady-State Error for Single-Phase Grid-Connected Inverters," *IEEE Trans. Smart Grid*, vol. 7, no. 1, pp. 74–83, Jan. 2016.
[24] C. Xie, X. Zhao, K. Li, D. Liu, J. M. Guerrero, and J. C. Vasquez, "Phase Compensated Reduced Order Generalized Integrators for Grid-Tied VSCs With Harmonics Compensation Capability," *IEEE Trans. Ind. Appl.*, vol. 54, no. 3, pp. 2568–2578, 2018.
[25] S. Golestan, J. M. Guerrero, and J. C. Vasquez, "An Adaptive Resonant Regulator for Single-Phase Grid-Tied VSCs," *IEEE Trans. Power Electron.*, vol. 33, no. 3, pp. 1867–1873, Mar. 2018.
[26] C. James and N. Sadegh, "Synthesis and Stability of A Multirate Repetitive Learning Controller," in *American Control Conference, 1999. Proceedings of the 1999*, 1999, pp. 358–362.
[27] B. Zhang, K. Zhou, and D. Wang, "Multirate Repetitive Control for PWM DC/AC Converters," *IEEE Trans. Ind. Electron.*, vol. 61, no. 6, pp. 2883–2890, Jun. 2014.
[28] C. Xie, X. Zhao, M. Savaghebi, L. Meng, J. M. Guerrero, and J. C. Vasquez, "Multirate Fractional-Order Repetitive Control of Shunt Active Power Filter Suitable for Microgrid Applications," *IEEE J. Emerg. Sel. Top. Power Electron.*, vol. 5, no. 2, pp. 809–819, Jun. 2017.
[29] A. Ghoshal and V. John, "High-Accuracy Multi-Rate Implementation of Resonant Integrator using FPGA," *IET Power Electron.*, vol. 10, no. 3, pp. 348–356, Mar. 2017.
[30] Gene F. Franklin, J. David Powell, and Michael Workman, *Digital Control of Dynamic Systems*, Third Edition. Addison Wesley Longman, 1998.
[31] X. Li, X. Wu, Y. Geng, X. Yuan, C. Xia, and X. Zhang, "Wide Damping Region for LCL-Type Grid-Connected Inverter With an Improved Capacitor-Current-Feedback Method," *IEEE Trans. Power Electron.*, vol. 30, no. 9, pp. 5247–5259, Sep. 2015.
[32] I. Etxeberria-Otadui, A. L. D. Heredia, H. Gaztanaga, S. Bacha, and M. R. Reyero, "A Single Synchronous Frame Hybrid (SSFH) Multifrequency Controller for Power Active Filters," *IEEE Trans. Ind. Electron.*, vol. 53, no. 5, pp. 1640–1648, Oct. 2006.
[33] D. Pérez-Estévez, J. Doval-Gandoy, A. G. Yepes, Ó. López, and F. Baneira, "Enhanced Resonant Current Controller for Grid-Connected Converters With LCL Filter," *IEEE Trans. Power Electron.*, vol. 33, no. 5, pp. 3765–3778, May 2018.
[34] F. Z. Peng, "Application Issues of Active Power Filters," *IEEE Ind. Appl. Mag.*, vol. 4, no. 5, pp. 21–30, Sep. 1998.

Chuan Xie (M'17) **received** the B.S. degree in automation engineering from the University of Electronic Science and Technology of China, Chengdu, China, and the Ph.D. degree in power electronics from Zhejiang University, Hangzhou, China, in 2007 and 2012, respectively.

Since 2012, he was a lecturer with the School of Automation Engineering at University of Electronic Science and Technology of China. From May 2015 to May 2016, he was a Visiting Scholar at the Department of Energy Technology, Aalborg University. His main research interests include digital control of power electronics, grid synchronization technology, distributed generation systems, microgrids and power quality.

Xin Zhao (S'15-M'17) received the B.S. and M.S. degrees in Power Electronics & Electrical Drives from Northwestern Polytechnical University, Xi'an, China, in 2010 and 2013, respectively, and the Ph.D. degree in electrical engineering from Aalborg University, Denmark, in 2017.

Since 2017, he has been with Northwestern Polytechnical University, Xi'an, China, as an Associate Professor. His research interests include power quality, distributed generation systems, and power electronic converter design, analysis and control.

Kai Li (M'16) received the B.S., M.S., and Ph.D. in Automation Engineering from the University of Electronic Science and Technology of China, Chengdu, China in 2006, 2009, and 2014, respectively.

From 2009 to 2016, he was an Assistant Professor with the School of Automation Engineering, University of Electronic Science and Technology of China, Chengdu, China. From 2016.2 to 2017.2, he was a Guest Researcher with the Department of Energy Technology, Aalborg University, Denmark. Since 2016, he has been an Associate Professor with the School of Automation Engineering, University of Electronic Science and Technology of China, Chengdu, China. His research interests include multilevel inverters, storage converters, and microgrids.

Jianxiao Zou (M'15) received the B.S., M.S., and Ph.D. degrees in control science and engineering from the University of Electronic Science and Technology of China (UESTC), Chengdu, China in 2000, 2003, and 2009, respectively.

He is currently a professor at UESTC, and served as Vice Dean of School of Automation Engineering from 2011. He was a visiting scholar of University of California, Berkeley in 2010 and senior visiting professor of Rutgers, the State University of New Jersey in 2014. His research interests include control theory and control engineering, renewable energy control technologies, intelligent information processing and control.

Josep M. Guerrero (S'01-M'04-SM'08 -F'15) received the B.S. degree in telecommunications engineering, the M.S. degree in electronics engineering, and the Ph.D. degree in power electronics from the Technical University of Catalonia, Barcelona, in 1997, 2000 and 2003, respectively. Since 2011, he has been a Full Professor with the Department of Energy Technology, Aalborg University, Denmark, where he is responsible for the Microgrid Research Program.

His research interests is oriented to different microgrid aspects, including power electronics, distributed energy-storage systems, hierarchical and cooperative control, energy management systems, and optimization of microgrids and islanded minigrids.